Modelling and Analysis of a Generalized Equivalent Magnetic Circuit Model for Moving Coil Electromagnetic Linear Actuators

Hao Yan, Jinshi Fang, Wenqing Ge, Geng Wang, Jiewei Chen, Cao Tan

***Abstract*—This paper proposes a generalized equivalent magnetic circuit model (EMCM) considering end-effect for a moving-coil electromagnetic linear actuator (MCELA). The model describes the magnetic networks in detail by incorporating the independent variable parallel branch number and constructing them as a function of variable branch number and geometric dimensions. An iterating method to update accurate relative permeability of the soft magnetic material under different working point is also taken into consideration. The comparison study of flux density and thrust force using FEM and EMCM demonstrates the effectiveness and computation efficiency of the proposed model. Additionally, a typical MCELA prototype is implemented to further validate the proposed EMCM. The proposed method can be used for the analysis and design of a wide range of electromagnetic actuators, in addition to its application to MCELA.**

***Index Terms*—Moving coil electromagnetic linear actuator, Analytical model, Equivalent magnetic circuit model, Material nonlinearity consideration**

I. Introduction

MOVING coil electromagnetic linear actuator (MCELA) is a type of electromagnetic driving device based on the Lorentz-Force principle, which can convert electrical energy directly into mechanical energy for linear motion without the participation of any intermediate conversion devices [1-3]. In comparison to other electromagnetic linear actuators(ELAs) [4,5], MCELA boasts a simple structure, fast response speed, and high motion accuracy. It has been employed in various applications, such as aerospace [6], vehicle [7] and fluid control systems [8].

To date, various methods have been employed for the preliminary design of ELAs, including up-to-date analytical [9], semi-analytical [10], and numerical [11] methods. Among them, the finite-element model (FEM) is used in the numerical method to obtain the results, which shows good agreement with experimental results. However, the FEM process is often time-consuming and computationally expensive, and requires model reconstruction when changing structural parameters. For the preliminary design of the MCELA, a general layout of the key machine parameters based on the application with basic design specifications is required [12]. Analytical methods are widely used as the solving tool in the preliminary design stage due to the large number of parameters that need to be determined, which can result in a huge number of possible solutions.

The analytical method used in the magnetic potential vector model (MPVM) is a parameter model that considers flux density distribution [13-15]. However, the MPVM adopts the assumption of infinite permeability for simplification, which means that it cannot model nonlinear material characteristics accurately. Another widely used analytical technique is the equivalent magnetic circuit model (EMCM), which can account for nonlinear material characteristics [16-18]. The Electromagnetic Circuit Method (EMCM) treats magnetic circuits as analogous to electric circuits, allowing for the calculation of electromagnetic field characteristics using electric circuit principles. However, due to the simplification of lumped parameters, it may not accurately reflect changes in flux density and thrust force, necessitating refined divisions. Therefore, EMCM is typically used for preliminary design and is then confirmed with FEM.

The objective of this study is to propose a generalized EMCM with time-efficient and precise calculations for a MCELA. Additionally, the magnetic field distribution, magnetic leakage of PM, and more refined equivalent magnetic circuits are described in the EMCM. The remaining contents of this paper are organized as follows: Section II introduces the structure of MCELA and provides the denoted structural parameters. The EMCM analytical model and its verification are presented. In Section III, prototype and test bench are developed, the experimental comparative study is performed. The paper is concluded with the Section IV.

Manuscript received January 12 2024; revised October 23, 2024. This study was supported by National Natural Science Foundation of China funded project (Grant No. 52375105 and Grant No. 52305265), Natural Science Foundation of Shandong Province (Grant No. ZR2022YQ51 and Grant No. ZR2023ME178).

Hao Yan is a lecturer in School of Transportation and Vehicle Engineering, Shandong University of Technology, Zibo 255000, Shandong, China (e-mail: utwg@hotmail.com).

Jinshi Fang is a postgraduate student in School of Transportation and Vehicle Engineering, Shandong University of Technology, Zibo 255000, Shandong, China (e-mail: fangjs7@163.com).

Wenqing Ge is a professor in School of Transportation and Vehicle Engineering, Shandong University of Technology, Zibo 255000, Shandong, China (e-mail: gwq@sdut.edu.cn).

Geng Wang is a lecturer in School of Transportation and Vehicle Engineering, Shandong University of Technology, Zibo 255000, Shandong, China (corresponding author to provide phone: +86 15695478898; e-mail: utwg@hotmail.com).

Jiewei Chen is a Ph.D. student in School of Transportation and Vehicle Engineering, Shandong University of Technology, Zibo 255000, Shandong, China (e-mail: c18337619637@163.com).

Cao Tan is a professor in School of Transportation and Vehicle Engineering, Shandong University of Technology, Zibo 255000, Shandong, China (e-mail: njusttancao@yeah.net).

II. Analytical Modeling of EMCM

A. Fundamental configuration of MCELA

The structure of proposed MCELA is shown in Fig. 1. It has a cylindrically symmetrical structure consists of stator part and moving part. The stator part is composed of the end covers, array of permanent magnets (PMs), outer yoke, and inner yoke. The moving part consists of the coil framework, coil and shaft output. The outer yoke carries several main PMs which are radially magnetized, and neighboring magnets are magnetized in the opposite directions to produce a nearly uniform distributed magnetic field perpendicular to the coil. Between two main PMs, there is an adjacent PM magnetized axially to form a Halbach magnet array to enhance the flux density in the air gap. The coils are wound in series on the coil framework with the polarity of the two neighboring coils reversed 180°. The thrust force is generated by the interaction of a magnetic fields and an excitation coil based on the Lorentz-Force principle. The magnitude and direction of the thrust force are determined by the magnitude and direction of armature current.

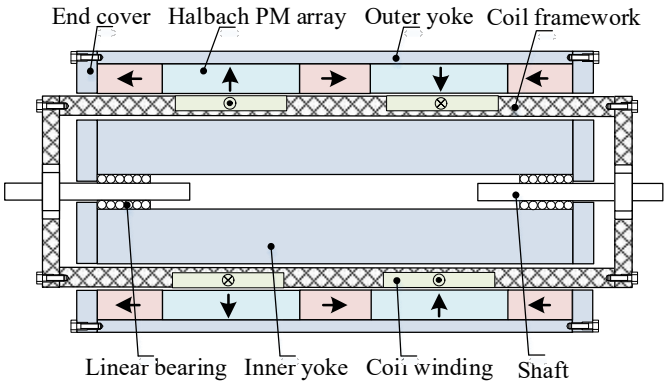

Fig. 1. Structure of MCELA.

In this study, the MCELA is applied to a direct-drive pumping system, thus requiring the MCELA to have sufficient thrust ant compact dimensions to overcome the hydrodynamic and inertial force at high frequencies. In addition, the high thrust linearity of the MCELA is required to achieve wide bandwidth and robust motion control. Therefore, all structural parameters used in the MCELA need to be organized and analyzed for engineering applications of direct-driven pump system. For further magnetic modeling and design, the MCELA with leading structural parameters denoted is shown in Fig. 2.

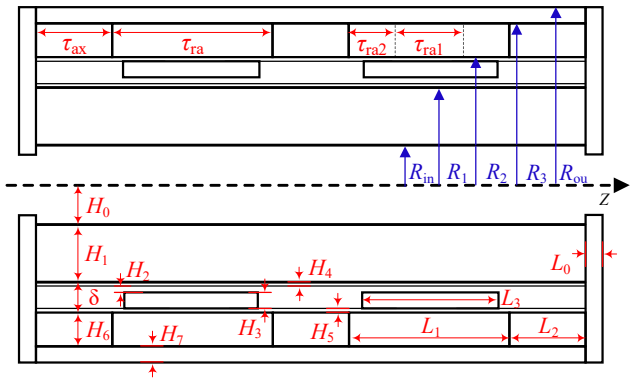

Fig. 2. Leading structural parameters of MCELA.

B. Geometry definitions and EMCM modeling

The EMCM of the proposed triple-pole MCELA is established, as shown in Fig. 3. Depending on the relative permeability, the EMCM is divided into four areas, which are presented by four different colors. The region of radially magnetized PMs is represented by the green areas, which are divided into two parts with a relative permeability of μ_r. The red areas represent the region of axially magnetized PMs with a relative permeability of μ_r. The whiter areas represent the region of the air-gap and the working range, which have a permeability is μ_0. The blue areas represent the region of the soft magnetic material and the relative permeability is μ_{rmi}.

Fig. 3 shows the symbols used in this study, including the absolute magnetomotive force, F, magnetic reluctance, R, and magnetic flux, Φ. The definitions of these symbols are defined as follows: F_k^n represents the magnetomotive force of PMs, R_{pk}^n represents the magnetic reluctance of PMs, R_{ak}^n represents the magnetic reluctance of the air gap, R_{bik}^n represents the magnetic reluctance of inner yoke, and Φ_{gk}^n represents the flux through the cover.

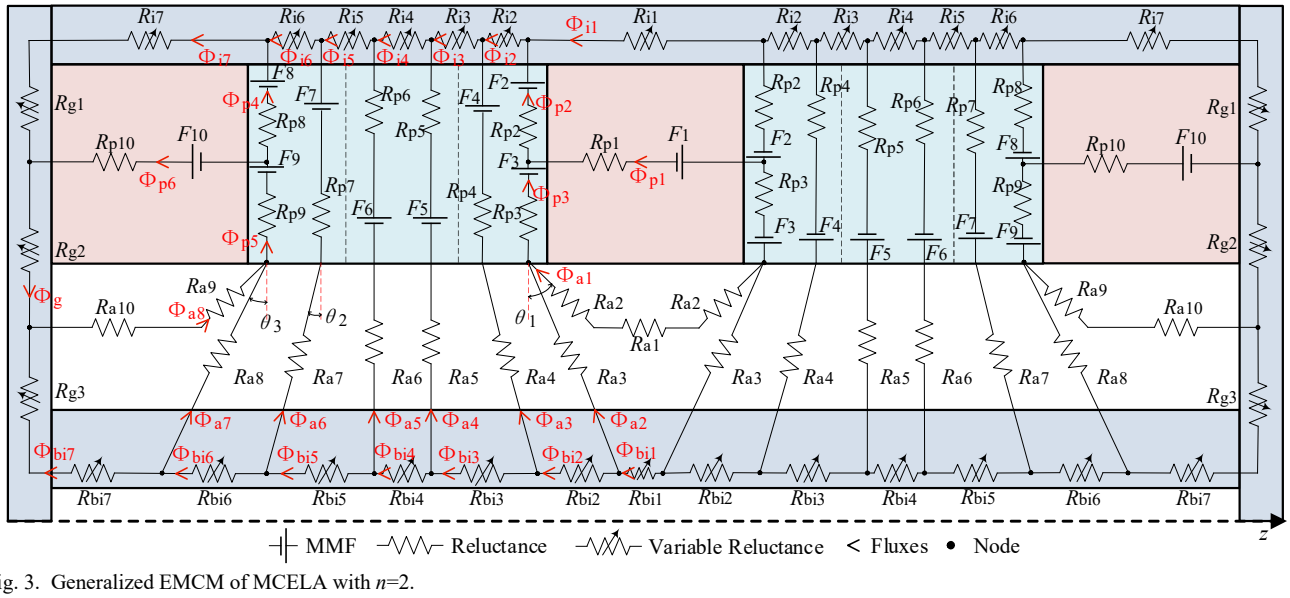

Fig. 3. Generalized EMCM of MCELA with n=2.

The symbol n represents the number of parallel branches of the magnetic induction line in PMs, which can be used to describe the precision of the model. The larger of n results in higher model precision and calculation accuracy, but also leads to higher computational costs. For clarity, the EMCM of n=2 is shown in fig. 3. The symbol k represents the number of nodes in each area. This is determined by the node arrangement and varies with n. It is important to note that, in order to maintain consistency for the subscripts and superscripts, all superscripts are n, and all subscripts are indexed from 1 to k.

For the sake of calculation convenience, the magnetic reluctance is expressed as the reciprocal of the magnetic permeance, which can be expressed as follows:

$$R^n = \frac{1}{P^n} \tag{1}$$

where P^n is the magnetic permeance of each part, which can be expressed as follows:

$$P^n = \mu_0 \mu^n \frac{S^n}{L^n} \tag{2}$$

where μ^n is the relative permeability between adjacent nodes, S^n is the cross-sectional area of magnetic conductance between adjacent nodes, and L^n is the thickness of the magnetic conductance between adjacent nodes.

The magnetomotive force of PMs can be expressed as follows:

$$F^n = H_c t^n \tag{3}$$

where H_c is the PM coercivity, and t^n is the thickness of PM. Based on the KCL/KVL method, the magnetomotive force is equivalent to voltage, magnetic reluctance is equivalent to resistance, and flux is equivalent to current. Therefore, flux can be calculated using Ohm's law, which is expressed as follows:

$$\Phi^n = \frac{F^n}{R^n} \tag{4}$$

In this study, the EMCM is expressed as a matrix, which can be solved by computer programming. The magnetic reluctances are arranged in a matrix of size $(9n+11) \times (9n+11)$ in a specific order, as follows:

$$\mathbf{R} = \begin{bmatrix} \left(\mathbf{R}_C^n\right)_{(6n+6)\times(9n+11)} \\ \left(\mathbf{R}_V^n\right)_{(3n+5)\times(9n+11)} \end{bmatrix}_{(9n+11)\times(9n+11)} \tag{5}$$

where the magnetic reluctance matrix $\mathbf{R}$ is divided into two submatrices, $\mathbf{R}_C^n$ and $\mathbf{R}_V^n$ respectively. The dimension of $\mathbf{R}_C^n$ is determined by the number of nodes in the model, and the dimension of $\mathbf{R}_V^n$ is determined by the number of independent closed loops within the model.

The matrix for magnetomotive force is expressed as follows:

$$\mathbf{F} = \begin{bmatrix} \left(\mathbf{F}_C^n\right)_{(6n+6)\times 1} \\ \left(\mathbf{F}_V^n\right)_{(3n+5)\times 1} \end{bmatrix}_{(9n+11)\times 1} \tag{6}$$

where $\mathbf{F}_C^n$ is determined by the number of nodes in the model, and the dimension of $\mathbf{F}_V^n$ is determined by the number of independent closed loops within the model. It should be noted that, the equation of KCL do not have magnetomotive force, so $\mathbf{F}_C^n = \mathbf{0}$.

The magnetic flux matrix of each branch is expressed as follows:

$$\mathbf{\Phi} = \begin{bmatrix} \left(\mathbf{\Phi}_{bi}^n\right)_{(3n+1)\times 1} \\ \left(\mathbf{\Phi}_a^n\right)_{(3n+2)\times 1} \\ \left(\mathbf{\Phi}_p^n\right)_{6\times 1} \\ \left(\mathbf{\Phi}_i^n\right)_{(3n+1)\times 1} \\ \left(\mathbf{\Phi}_g^n\right)_{1\times 1} \end{bmatrix}_{(9n+11)\times 1} \tag{7}$$

where the submatrices $\mathbf{\Phi}_{bi}^n$, $\mathbf{\Phi}_a^n$, $\mathbf{\Phi}_p^n$, and $\mathbf{\Phi}_i^n$ are the fluxes through each area, with their dimensions depending on the number of branches in the area. Based on the Eq. (4), the matrix $\mathbf{\Phi}$ can be obtained using the following equation:

$$\mathbf{\Phi} = \mathbf{R}^{-1}\mathbf{F} \tag{8}$$

where matrix $\mathbf{R}^{-1}$ is the inverse of matrix $\mathbf{R}$.

In this study, the calculated flux density is contributed soled by PMs due to the slotless structure of MCELA, since the flux generated by the current is much smaller. The circumferential symmetrical structure of MCELA ensures that the fixed network does not affect the accuracy of the results. Any machine with slot-less structure can be modeled, and the EMCM can be viewed as a function of the independent variable n. A detailed modeling process is provided in the Appendix.

A. Nonlinear Material Consideration

The yokes are made of the soft iron material which has a nonlinear B-H relationship. The permeability can vary significantly with the flux density. Therefore, EMCM introduces nonlinear permeance, where the relative recoil permeability is determined iteratively according to the nonlinear B-H characteristic. The relationship between relative permeability and flux density in soft iron can be calculated by the function as follows:

$$\mu_{\text{rmi}} = \left(\frac{B_0}{\mu_0 H_0}\right)\left(\frac{1}{1+(B/B_0)^{v-1}}\right) \tag{9}$$

where B_0, H_0 and v are constants related to materials. In this study, the soft iron material S10C with constants B_0= 1.2, H_0=190, and v = 12 is employed. The μ_{rmi}-B curve of S10C is shown in Fig. 4.

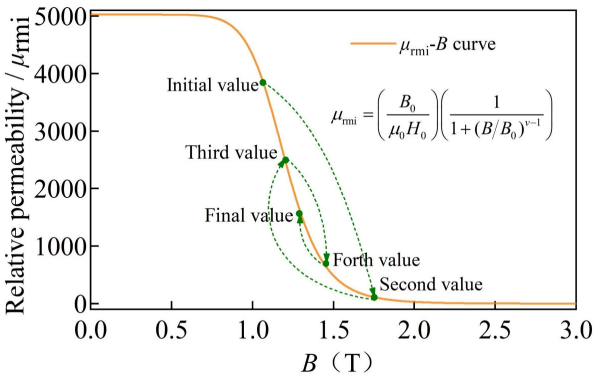

Fig. 4. Relative permeability curve of S10C.

To enhance the precision of EMCM, it is essential to update the variable reluctance through an iterative process.

The specific iterative updating process is shown in Fig. 4. Initially, a relative permeability is assigned to calculate the variable reluctance, and the initial magnetic flux density can be obtained using Eq. (9). Subsequently, the relative permeability is iterated and updated using the following function:

$$\mu_{\mathrm{rmi}}^{(k+1)} = \left(\frac{B_0}{\mu_0 H_0}\right)\left(\frac{1}{1+(B^{(k)}/B_0)^{v-1}}\right) \tag{10}$$

Next, the updated relative permeability is inputted into the EMCM and replaces the previous value. The calculation process continues to iterate until the convergence stop condition is reached. The convergence stop condition can be expressed as the constraint on the variation of permeability during the last two iterations:

$$\max\left|\frac{\mu_{\mathrm{rmi}}^{(k+1)} - \mu_{\mathrm{rmi}}^{(k)}}{\mu_{\mathrm{rmi}}^{(k)}}\right| \le \varepsilon \tag{11}$$

where ε is a small positive constant.

To solve the matrix **Φ,** the matrix **R** is required, which has many elements that are functions of the relative permeability. The relative permeability is, in turn, a function of the magnetic flux density **B**. Any nonlinear solution algorithm can be used to solve the above nonhomogeneous system of equations. In this study, the Jacobi iterative method was adopted.

B. Comparison of flux density

The EMCM should be verified before it is used for design. The model is verified by FEM method in the present study, and the model parameters selected for comparison with FEM and EMCM are listed in Table 1. To compare with the EMCM model, three positions located in the middle of air-gap, outer yoke, and inner yoke are adopted.

TABLE I
VERIFICATION STRUCTURAL PARAMETERS

Symbol	Parameter	Value
H_0	Thickness of inner yoke gap	5.0 mm
H_1	Thickness of inner yoke	15.5 mm
H_3	Thickness of coil	3.0 mm
H_6	Thickness of PMs	6.5 mm
H_7	Thickness of outer yoke	4.0 mm
L_1 / τ_{ra}	Length of radially magnetized PMs	16.0 mm
L_2 / τ_{ax}	Length of axially magnetized PMs	8.0 mm
L_3	Length of each coil	6.0 mm

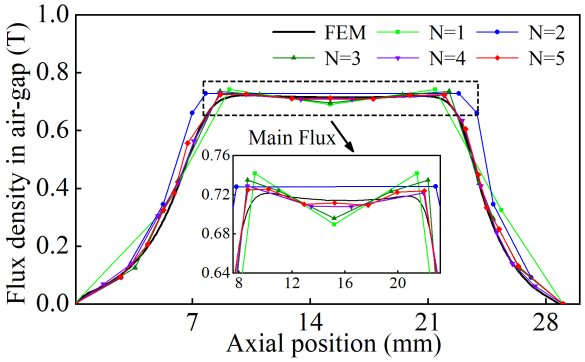

Fig. 5. Comparison of flux density in air-gap by EMCM and FEM.

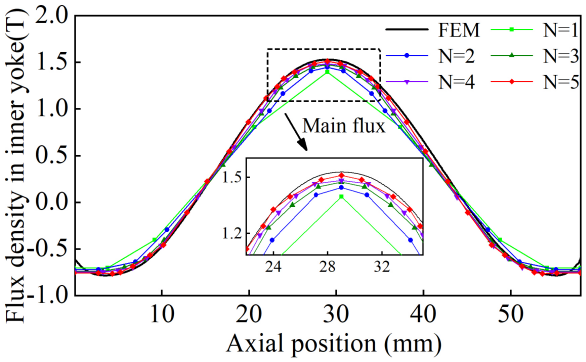

Fig. 6. Comparison of flux density in inner yoke by EMCM and FEM.

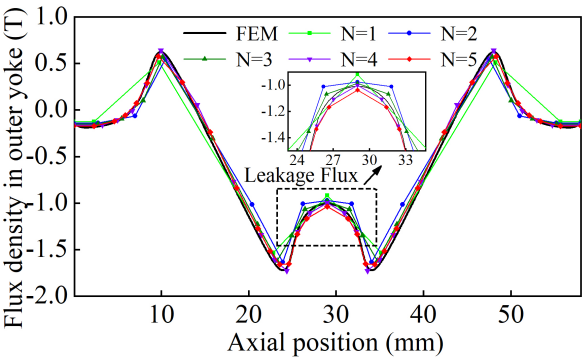

Fig. 7. Comparison of flux density in outer yoke by EMCM and FEM.

The comparisons of flux density of EMCM and FEM in air-gap, outer yoke, and inner yoke are shown in Fig.5, Fig. 6, and Fig. 7, respectively. It can be indicated that the results of EMCM are in good agreement with FEM in different comparison regions, which can validate the correctness and precision of the EMCM. Additionally, the calculation accuracy of EMCM increases with the number of parallel branches *n*, especially for the middle position of radially magnetized PMs. The reason for this difference is that FEM calculates values for individual nodes, while EMCM calculates lumped parameters. The EMCM calculation divides the total flux density by the cross-sectional area, providing an average flux density for the sectional area. As the number of parallel branches *n* increases, the solution region becomes more refined, resulting in a more uniform flux distribution. This explains why larger values of *n* provide better agreement. Although the calculation results for small value *n* by EMCM show deviation in the flux distribution, they agree well with the FEM results at the peak value. Typically, only the maximum flux densities in yokes are of interest for avoiding saturation during design.

C. Comparison of thrust force

The comparison of thrust force versus displacement position with different excitation currents calculated by EMCM and FEM is shown in Fig. 8. The results of thrust force by EMCM are consistent with the results of flux distribution. But at the endpoint of the stroke the thrust force results of EMCM show slightly decline with the FEM because the armature reaction is not calculated. When the excitation current is 15 A, the average thrust force of EMCM and FEM is 452.81N and 451.97N, respectively. The results of average thrust force are with highly accuracy due to the periodicity of the armature reaction. The comparison of flux density and thrust force by EMCM and FEM indicates that the accuracy of EMCM is acceptable for design of MCELA.

In addition, it is worth noting that the calculation time for 2D FEM by JMAG-Designer takes more than 5 minutes with the element number of 81814, the nodes number of 52763, and the calculation steps of 41, without considering the time required for reconstructing the model. However, the EMCM proposed in this manuscript only requires 3.7 seconds, making it particularly suitable for the design of MCELA to shorten computation time.

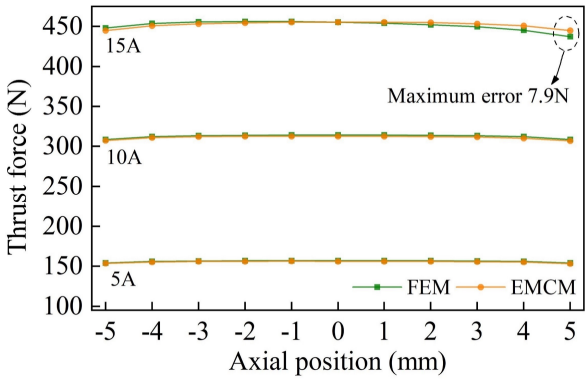

Fig. 8. Comparison of thrust force by EMCM and FEM.

III. Experimental Verification and Discussion

A. Experimental setup and prototype

To assess the effectiveness of the design and the performance of the prototype, a performance test system for the MCELA was established. The system is illustrated in Figures 9 and 10. Figure 9 provides detailed structural features of the unit, while Figure 10 shows the setup of the test platform.

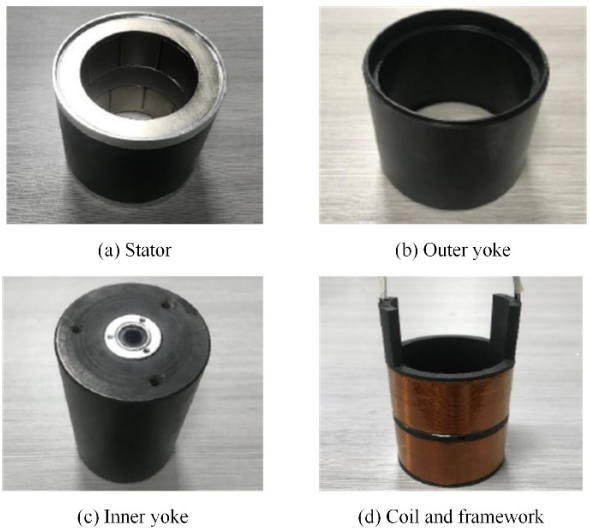

Fig. 9. prototype and components:(a) Stator (b) Outer yoke (c) Inner yoke (d) Coil and framework

As shown in Fig. 10 (a), an experimental setup for air-gap flux density measurement is established. A Hall probe of the three-dimensional Gauss meter is mounted on the hold cage to collect the measured data of fluxes at different axial positions within the MCELA. The Gauss meter is linked to host for data processing and image editing. The experiment is carried out without current load, the position sample interval is 2 mm. Fig. 10 (b) shows the test bench used to measure the total thrust force as the mover position varies with different current levels. The real-time digital signal controller chosen for this experiment is the fixed-point DSP TMS320F2812. The following signals including the coil current, the coil voltage, the position of the moving part, and the thrust force are fed back to the host for data processing.

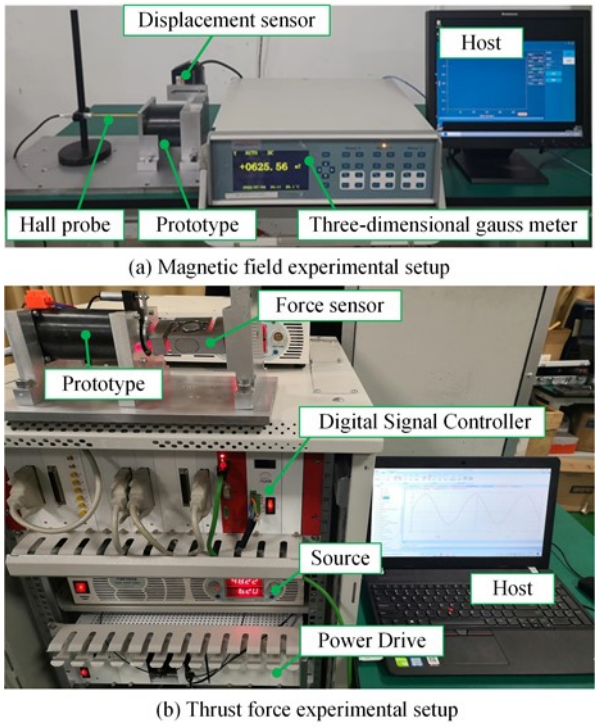

Fig. 10. Experimental setup and prototype.

B. Experiment of air-gap flux density

In this study, the accuracy and precision of the EMCM results increase with n. In order to simplify the test verification process, only the results when n is 5 are verified. Experimental validation of the air-gap flux density is the comparison of EMCM, FEM and experiment results.

When the mover is fixed without any current input, the flux density along the air gap is tested. The open-circuit flux density in EMCM, FEM, and experiments with high consistency and accuracy is shown in Fig. 11. The results by EMCM are close to the FEM curve, although some errors still exist due to model simplification, measurement errors and manufacturing errors. Fig. 12 clearly shows the discrepancy between the air gap flux density calculated by the FEM method and the EMCM method, as well as the experimental measurement of the air gap flux density results. Significantly, in the working region where the air gap flux density changes less, the error with the experimental measurement results is smaller.

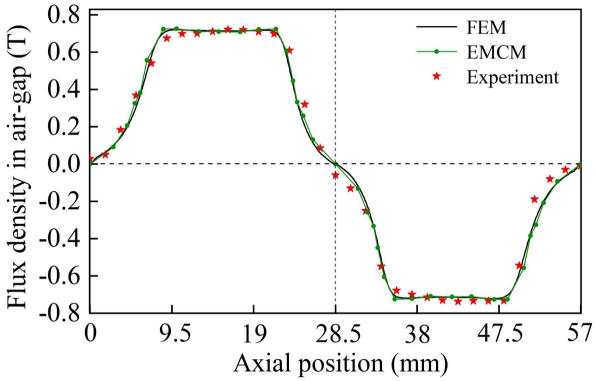

Fig. 11. Analytical and measured air-gap flux density characteristics.

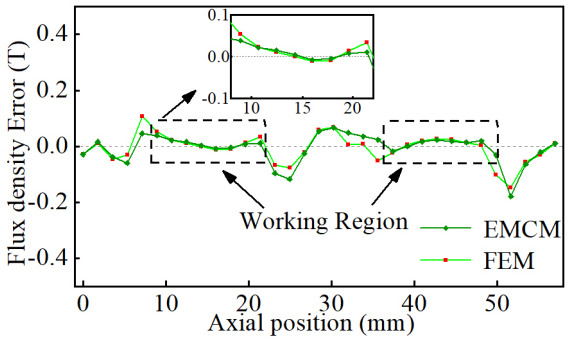

Fig. 12. Errors of FEM calculations and EMCM calculations versus experimental measurements of air-gap flux density.

C. Experiment of thrust force characteristic

The experimental results confirm the accuracy of the EMCM results, as shown in Figure 13, which shows the static thrust force results obtained by EMCM and the corresponding experimental measurements for various positions and current levels. The thrust force values are dependent on the displacement position, and the thrust force versus displacement position exhibits high-linearity. The results show a discrepancy of thrust force under the rated current of 15A varying of 20.09 N at most (error is less than 4.5%). The thrust force is proportional to the injected current, but the errors between EMCM and experimental results increase with the injected current. This is attributed to a slight asymmetry in the magnetic circuit of the prototype and the absence of the armature reaction in EMCM.

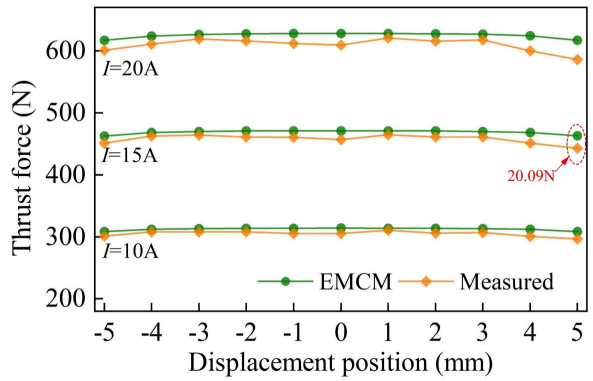

Fig. 13. The thrust force versus position of MCELA prototype.

IV. Conclusion

In this paper, a generalized equivalent magnetic circuit model is developed and applied to a moving-coil electromagnetic linear actuator used in a direct-drive pump. Conclusions can be drawn as follows.

(1) The results of the proposed combinatorial analytical model and FEM method are with high consistency, which means that it can be acceptable for further design of MCELA.

(2) The experimental and analytical results agree well with each other regarding the thrust force characteristic, which further validates the correctness of the proposed EMCM.

(3) As the number of the parallel branches n increases, the solution region of EMCM becomes more refined, resulting in a more uniform flux distribution and higher solving accuracy.

Appendix

$$F_1^{\mathrm{n}} = H_{\mathrm{c}}\tau_{\mathrm{ax}}$$

$$F_2^{\mathrm{n}} = H_{\mathrm{c}}\left(1-k_{\mathrm{r}}\right)\left(R_3-R_2\right)$$

$$F_3^{\mathrm{n}} = H_{\mathrm{c}}k_{\mathrm{r}}\left(R_3-R_2\right)$$

$$F_4^{\mathrm{n}} = H_{\mathrm{c}}\left(R_3-R_2\right)$$

$$P_{\mathrm{p1}}^{\mathrm{n}} = \mu_0\mu_{\mathrm{r}}\frac{\pi\left(R_3^2-R_2^2\right)}{\tau_{\mathrm{ax}}}$$

$$P_{\mathrm{p2}}^{\mathrm{n}} = \mu_0\mu_{\mathrm{r}}\frac{\pi\tau_{\mathrm{ra2}}\left[R_2+R_3+\left(R_3-R_2\right)k_{\mathrm{r}}\right]}{2\left(R_3-R_2\right)\left(1-k_{\mathrm{r}}\right)}$$

$$P_{\mathrm{p4}}^{\mathrm{n}} = \mu_0\mu_{\mathrm{r}}\frac{\pi\tau_{\mathrm{ra1}}\left(R_2+R_3\right)}{2\left(R_3-R_2\right)}$$

$$P_{\mathrm{p3}}^{\mathrm{n}} = \mu_0\mu_{\mathrm{r}}\frac{\pi\tau_{\mathrm{ra2}}\left[2R_2+\left(R_3-R_2\right)k_{\mathrm{r}}\right]}{2\left(R_3-R_2\right)k_{\mathrm{r}}}$$

$$P_{\mathrm{a1}}^{\mathrm{n}} = \mu_0\frac{\pi\left(R_2^2-R_1^2\right)}{\tau_{\mathrm{ax}}+\dfrac{\tau_{\mathrm{ra2}}}{n}-\left(R_2-R_1\right)\tan\theta_1}$$

$$P_{\mathrm{a2}}^{\mathrm{n}} = \mu_0\frac{\pi\tau_{\mathrm{ra2}}\left(R_1+3R_2\right)\cos\theta_1}{n\left(R_2-R_1\right)}$$

$$P_{\mathrm{a3}}^{\mathrm{n}} = \mu_0\frac{\pi\tau_{\mathrm{ra2}}\left(R_2+R_1\right)\cos\theta_3}{n\left(R_2-R_1\right)}$$

$$P_{\mathrm{a4}}^{\mathrm{n}} = \mu_0\frac{\pi\tau_{\mathrm{ra2}}\left(R_2+R_1\right)\cos\theta_2}{n\left(R_2-R_1\right)}$$

$$P_{\mathrm{a5}}^{\mathrm{n}} = \mu_0\frac{\pi\tau_{\mathrm{ra1}}\left(R_2+R_1\right)}{n\left(R_2-R_1\right)}$$

$$P_{\mathrm{g1}}^{\mathrm{n}} = \mu_0\mu_{\mathrm{rmi}}\frac{\pi\delta\left[2R_2+R_3+R_{\mathrm{ou}}+2\left(R_3-R_2\right)k_{\mathrm{r}}\right]}{R_3+R_{\mathrm{ou}}-2R_2+2\left(R_3-R_2\right)k_{\mathrm{r}}}$$

$$P_{\mathrm{g2}} = \mu_0\mu_{\mathrm{rmi}}\frac{\pi\delta\left[3R_2+R_1+2\left(R_3-R_2\right)k_{\mathrm{r}}\right]}{2R_2+2\left(R_3-R_2\right)k_{\mathrm{r}}-\left(R_2+R_1\right)}$$

$$P_{\mathrm{g3}} = \mu_0\mu_{\mathrm{rmi}}\frac{\pi\delta\left[2R_2+4R_1-2R_{\mathrm{in}}\right]}{R_2+R_{\mathrm{in}}}$$

$$P_{\mathrm{i1}}^{\mathrm{n}} = \mu_0\mu_{\mathrm{rmi}}\frac{\pi\left(R_{\mathrm{ou}}^2-R_3^2\right)}{\tau_{\mathrm{ax}}+\dfrac{\tau_{\mathrm{ra2}}}{n}}$$

$$P_{\mathrm{i2}}^{\mathrm{n}} = \mu_0\mu_{\mathrm{rmi}}\frac{\pi\left(R_{\mathrm{ou}}^2-R_3^2\right)}{\dfrac{\tau_{\mathrm{ra2}}}{n}}$$

$$P_{\mathrm{i3}}^{\mathrm{n}} = \mu_0\mu_{\mathrm{rmi}}\frac{\pi\left(R_{\mathrm{ou}}^2-R_3^2\right)}{\dfrac{1}{2n}\left(\tau_{\mathrm{ra1}}+\tau_{\mathrm{ra2}}\right)}$$

$$P_{\mathrm{i4}}^{\mathrm{n}} = \mu_0\mu_{\mathrm{rmi}}\frac{\pi\left(R_{\mathrm{ou}}^2-R_3^2\right)}{\dfrac{\tau_{\mathrm{ra1}}}{n}}$$

$$P_{\mathrm{bi1}}^{\mathrm{n}}=\mu_0\mu_{\mathrm{rmi}}\frac{\pi\left(R_1^2-R_{\mathrm{in}}^2\right)}{\tau_{\mathrm{ax}}+\dfrac{\tau_{\mathrm{ra2}}}{n}-2\left(R_2-\dfrac{R_1+3R_{\mathrm{in}}}{2}\right)\tan\theta_2}$$

$$P_{\mathrm{bi2}}^{\mathrm{n}}=\mu_0\mu_{\mathrm{rmi}}\frac{\pi\left(R_1^2-R_{\mathrm{in}}^2\right)}{\dfrac{\tau_{\mathrm{ra2}}}{n}+\left(R_2-\dfrac{R_1+3R_{\mathrm{in}}}{2}\right)\left(\tan\theta_2-\tan\theta_1\right)}$$

$$P_{\mathrm{bi3}}^{\mathrm{n}}=\mu_0\mu_{\mathrm{rmi}}\frac{\pi\left(R_1^2-R_{\mathrm{in}}^2\right)}{\dfrac{1}{2n}\left(\tau_{\mathrm{ra1}}+\tau_{\mathrm{ra2}}\right)+\left[R_2-\left(\dfrac{R_1+3R_{\mathrm{in}}}{2}\right)\right]\tan\theta_1}$$

$$P_{\mathrm{bi4}}^{\mathrm{n}}=\mu_0\mu_{\mathrm{rmi}}\frac{\pi\left(R_1^2-R_{\mathrm{in}}^2\right)}{\dfrac{\tau_{\mathrm{ra1}}}{n}}$$

$$\boldsymbol{\Phi}_{\mathrm{bi}}^{\mathrm{n}}=\begin{bmatrix}\boldsymbol{\Phi}_{\mathrm{bi1}} & \boldsymbol{\Phi}_{\mathrm{bi2}} & \boldsymbol{\Phi}_{\mathrm{bi3}} & \boldsymbol{\Phi}_{\mathrm{bi4}} & \boldsymbol{\Phi}_{\mathrm{bi5}} & \boldsymbol{\Phi}_{\mathrm{bi6}} & \boldsymbol{\Phi}_{\mathrm{bi7}}\end{bmatrix}^{\mathrm{T}}$$

$$\boldsymbol{\Phi}_{\mathrm{a}}^{\mathrm{n}}=\begin{bmatrix}\boldsymbol{\Phi}_{\mathrm{a1}} & \boldsymbol{\Phi}_{\mathrm{a2}} & \boldsymbol{\Phi}_{\mathrm{a3}} & \boldsymbol{\Phi}_{\mathrm{a4}} & \boldsymbol{\Phi}_{\mathrm{a5}} & \boldsymbol{\Phi}_{\mathrm{a6}} & \boldsymbol{\Phi}_{\mathrm{a7}} & \boldsymbol{\Phi}_{\mathrm{a8}}\end{bmatrix}^{\mathrm{T}}$$

$$\boldsymbol{\Phi}_{\mathrm{p}}^{\mathrm{n}}=\begin{bmatrix}\boldsymbol{\Phi}_{\mathrm{p1}} & \boldsymbol{\Phi}_{\mathrm{p2}} & \boldsymbol{\Phi}_{\mathrm{p3}} & \boldsymbol{\Phi}_{\mathrm{p4}} & \boldsymbol{\Phi}_{\mathrm{p5}} & \boldsymbol{\Phi}_{\mathrm{p6}}\end{bmatrix}^{\mathrm{T}}$$

$$\boldsymbol{\Phi}_{\mathrm{i}}^{\mathrm{n}}=\begin{bmatrix}\boldsymbol{\Phi}_{\mathrm{i1}} & \boldsymbol{\Phi}_{\mathrm{i2}} & \boldsymbol{\Phi}_{\mathrm{i3}} & \boldsymbol{\Phi}_{\mathrm{i4}} & \boldsymbol{\Phi}_{\mathrm{i5}} & \boldsymbol{\Phi}_{\mathrm{i6}} & \boldsymbol{\Phi}_{\mathrm{i7}}\end{bmatrix}^{\mathrm{T}}$$

$$\boldsymbol{\Phi}_{\mathrm{g}}^{\mathrm{n}}=\begin{bmatrix}\boldsymbol{\Phi}_{\mathrm{g}}\end{bmatrix}$$

$$\mathbf{F}_{\mathrm{C}}^{\mathrm{n}}=\begin{bmatrix}0\end{bmatrix}_{(6N+6)\times 1}$$

$$\mathbf{F}_{\mathrm{V}}^{\mathrm{n}}=\begin{bmatrix}F_1-2F_2 & -F_1-2F_3 & 0 & 0 & 0 & 0 & 0 & 0 & F_8-F_{10} & F_9+F_{10} & 0\end{bmatrix}^{\mathrm{T}}$$

$$\mathbf{R}_{\mathrm{C}}^{\mathrm{n}}=\begin{bmatrix}
1 & -1 & 0 & 0 & 0 & 0 & 0 & 0 & -1 & 0 & 0 & 0 & 0 & 0 & 0 & 0 & 0 & 0 & 0 & 0 & 0 & 0 & 0 & 0 & 0 & 0 & 0 & 0 & 0 \\
0 & 1 & -1 & 0 & 0 & 0 & 0 & 0 & 0 & -1 & 0 & 0 & 0 & 0 & 0 & 0 & 0 & 0 & 0 & 0 & 0 & 0 & 0 & 0 & 0 & 0 & 0 & 0 & 0 \\
0 & 0 & 1 & -1 & 0 & 0 & 0 & 0 & 0 & 0 & -1 & 0 & 0 & 0 & 0 & 0 & 0 & 0 & 0 & 0 & 0 & 0 & 0 & 0 & 0 & 0 & 0 & 0 & 0 \\
0 & 0 & 0 & 1 & -1 & 0 & 0 & 0 & 0 & 0 & 0 & -1 & 0 & 0 & 0 & 0 & 0 & 0 & 0 & 0 & 0 & 0 & 0 & 0 & 0 & 0 & 0 & 0 & 0 \\
0 & 0 & 0 & 0 & 1 & -1 & 0 & 0 & 0 & 0 & 0 & 0 & -1 & 0 & 0 & 0 & 0 & 0 & 0 & 0 & 0 & 0 & 0 & 0 & 0 & 0 & 0 & 0 & 0 \\
0 & 0 & 0 & 0 & 0 & 1 & -1 & 0 & 0 & 0 & 0 & 0 & 0 & -1 & 0 & 0 & 0 & 0 & 0 & 0 & 0 & 0 & 0 & 0 & 0 & 0 & 0 & 0 & 0 \\
0 & 0 & 0 & 0 & 0 & 0 & 0 & 1 & 1 & 0 & 0 & 0 & 0 & 0 & 0 & 0 & 0 & -1 & 0 & 0 & 0 & 0 & 0 & 0 & 0 & 0 & 0 & 0 & 0 \\
0 & 0 & 0 & 0 & 0 & 0 & 0 & 0 & 0 & 0 & 0 & 0 & 0 & 1 & 1 & 0 & 0 & 0 & 0 & -1 & 0 & 0 & 0 & 0 & 0 & 0 & 0 & 0 & 0 \\
0 & 0 & 0 & 0 & 0 & 0 & 1 & 0 & 0 & 0 & 0 & 0 & 0 & 0 & 0 & -1 & 0 & 0 & 0 & 0 & 0 & 0 & 0 & 0 & 0 & 0 & 0 & 0 & 1 \\
0 & 0 & 0 & 0 & 0 & 0 & 0 & 0 & 0 & 0 & 0 & 0 & 0 & 0 & 0 & 0 & -1 & -1 & 1 & 0 & 0 & 0 & 0 & 0 & 0 & 0 & 0 & 0 & 0 \\
0 & 0 & 0 & 0 & 0 & 0 & 0 & 0 & 0 & 0 & 0 & 0 & 0 & 0 & 0 & 0 & 0 & 0 & 0 & -1 & 1 & -1 & 0 & 0 & 0 & 0 & 0 & 0 & 0 \\
0 & 0 & 0 & 0 & 0 & 0 & 0 & 0 & 0 & 0 & 0 & 0 & 0 & 0 & 0 & 0 & 0 & 0 & 0 & 0 & 0 & 1 & 0 & 0 & 0 & 0 & 0 & 1 & -1 \\
0 & 0 & 0 & 0 & 0 & 0 & 0 & 0 & 0 & 0 & 0 & 0 & 0 & 0 & 0 & 0 & 0 & 1 & 0 & 0 & 0 & 0 & 1 & -1 & 0 & 0 & 0 & 0 & 0 \\
0 & 0 & 0 & 0 & 0 & 0 & 0 & 0 & 0 & 1 & 0 & 0 & 0 & 0 & 0 & 0 & 0 & 0 & 0 & 0 & 0 & 0 & 0 & 1 & -1 & 0 & 0 & 0 & 0 \\
0 & 0 & 0 & 0 & 0 & 0 & 0 & 0 & 0 & 0 & 1 & 0 & 0 & 0 & 0 & 0 & 0 & 0 & 0 & 0 & 0 & 0 & 0 & 0 & 1 & -1 & 0 & 0 & 0 \\
0 & 0 & 0 & 0 & 0 & 0 & 0 & 0 & 0 & 0 & 0 & 1 & 0 & 0 & 0 & 0 & 0 & 0 & 0 & 0 & 0 & 0 & 0 & 0 & 0 & 1 & -1 & 0 & 0 \\
0 & 0 & 0 & 0 & 0 & 0 & 0 & 0 & 0 & 0 & 0 & 0 & 1 & 0 & 0 & 0 & 0 & 0 & 0 & 0 & 0 & 0 & 0 & 0 & 0 & 0 & 1 & -1 & 0
\end{bmatrix}$$

$$\mathbf{R}_{\mathrm{C}}^{\mathrm{n}}=\begin{bmatrix}
0 & 0 & 0 & 0 & 0 & 0 & 0 & 0 & 0 & 0 & 0 & 0 & 0 & 0 & 0 & \frac{-1}{P_{\mathrm{p1}}} & \frac{-2}{P_{\mathrm{p2}}} & 0 & 0 & 0 & 0 & \frac{1}{P_{\mathrm{i1}}} & 0 & 0 & 0 & 0 & 0 & 0 & 0 \\
0 & 0 & 0 & 0 & 0 & 0 & 0 & -\frac{1}{P_{\mathrm{a1}}}-\frac{2}{P_{\mathrm{a2}}} & 0 & 0 & 0 & 0 & 0 & 0 & 0 & 0 & \frac{1}{P_{\mathrm{p1}}} & 0 & \frac{-2}{P_{\mathrm{p3}}} & 0 & 0 & 0 & 0 & 0 & 0 & 0 & 0 & 0 & 0 \\
\frac{-1}{P_{\mathrm{bi1}}} & 0 & 0 & 0 & 0 & 0 & 0 & \frac{1}{P_{\mathrm{a1}}}+\frac{2}{P_{\mathrm{a2}}} & \frac{-2}{P_{\mathrm{a3}}} & 0 & 0 & 0 & 0 & 0 & 0 & 0 & 0 & 0 & 0 & 0 & 0 & 0 & 0 & 0 & 0 & 0 & 0 & 0 & 0 \\
0 & \frac{-1}{P_{\mathrm{bi2}}} & 0 & 0 & 0 & 0 & 0 & 0 & \frac{1}{P_{\mathrm{a3}}} & -\frac{1}{P_{\mathrm{a4}}}-\frac{1}{P_{\mathrm{p4}}} & 0 & 0 & 0 & 0 & 0 & 0 & \frac{1}{P_{\mathrm{p2}}} & \frac{1}{P_{\mathrm{p3}}} & 0 & 0 & 0 & 0 & \frac{1}{P_{\mathrm{i2}}} & 0 & 0 & 0 & 0 & 0 \\
0 & 0 & \frac{-1}{P_{\mathrm{bi3}}} & 0 & 0 & 0 & 0 & 0 & 0 & \frac{1}{P_{\mathrm{a4}}}+\frac{1}{P_{\mathrm{p4}}} & -\frac{1}{P_{\mathrm{a5}}}-\frac{1}{P_{\mathrm{p5}}} & 0 & 0 & 0 & 0 & 0 & 0 & 0 & 0 & 0 & 0 & 0 & 0 & \frac{1}{P_{\mathrm{i3}}} & 0 & 0 & 0 & 0 \\
0 & 0 & 0 & \frac{-1}{P_{\mathrm{bi4}}} & 0 & 0 & 0 & 0 & 0 & 0 & \frac{1}{P_{\mathrm{a5}}}+\frac{1}{P_{\mathrm{p5}}} & -\frac{1}{P_{\mathrm{a6}}}-\frac{1}{P_{\mathrm{p6}}} & 0 & 0 & 0 & 0 & 0 & 0 & 0 & 0 & 0 & 0 & 0 & \frac{1}{P_{\mathrm{i4}}} & 0 & 0 & 0 & 0 \\
0 & 0 & 0 & 0 & \frac{-1}{P_{\mathrm{bi5}}} & 0 & 0 & 0 & 0 & 0 & 0 & \frac{1}{P_{\mathrm{a6}}}+\frac{1}{P_{\mathrm{p6}}} & -\frac{1}{P_{\mathrm{a7}}}-\frac{1}{P_{\mathrm{p7}}} & 0 & 0 & 0 & 0 & 0 & 0 & 0 & 0 & 0 & 0 & 0 & \frac{1}{P_{\mathrm{i5}}} & 0 & 0 & 0 \\
0 & 0 & 0 & 0 & 0 & \frac{-1}{P_{\mathrm{bi6}}} & 0 & 0 & 0 & 0 & 0 & 0 & \frac{1}{P_{\mathrm{a7}}}+\frac{1}{P_{\mathrm{p7}}} & \frac{-1}{P_{\mathrm{a8}}} & 0 & 0 & 0 & 0 & \frac{-1}{P_{\mathrm{p8}}} & \frac{-1}{P_{\mathrm{p9}}} & 0 & 0 & 0 & 0 & 0 & \frac{1}{P_{\mathrm{i6}}} & 0 & 0 \\
0 & 0 & 0 & 0 & 0 & 0 & 0 & 0 & 0 & 0 & 0 & 0 & 0 & \frac{1}{P_{\mathrm{a8}}} & -\frac{1}{P_{\mathrm{a9}}}-\frac{1}{P_{\mathrm{a10}}} & 0 & 0 & 0 & 0 & \frac{-1}{P_{\mathrm{p8}}} & 0 & \frac{-1}{P_{\mathrm{p10}}} & 0 & 0 & 0 & 0 & 0 & \frac{1}{P_{\mathrm{i7}}}+\frac{1}{P_{\mathrm{g1}}} & 0 \\
0 & 0 & 0 & 0 & 0 & 0 & 0 & 0 & 0 & 0 & 0 & 0 & 0 & 0 & \frac{1}{P_{\mathrm{a9}}}+\frac{1}{P_{\mathrm{a10}}} & 0 & 0 & 0 & 0 & \frac{1}{P_{\mathrm{p9}}} & \frac{1}{P_{\mathrm{p10}}} & 0 & 0 & 0 & 0 & 0 & 0 & 0 & \frac{1}{P_{\mathrm{g2}}} \\
0 & 0 & 0 & 0 & 0 & 0 & \frac{1}{P_{\mathrm{bi7}}}+\frac{1}{P_{\mathrm{g3}}} & 0 & 0 & 0 & 0 & 0 & 0 & \frac{1}{P_{\mathrm{a8}}} & -\frac{1}{P_{\mathrm{a9}}}-\frac{1}{P_{\mathrm{a10}}} & 0 & 0 & 0 & 0 & 0 & 0 & 0 & 0 & 0 & 0 & 0 & 0 & 0 & 0
\end{bmatrix}$$

REFERENCES

[1] G. Wang, Z. Lyu, R. Gao et al., "Optimization method for a moving-coil electromagnetic linear actuator using an improved Macaca thietanes behavior-based hierarchical GA–PSO algorithm," Structural and Multidisciplinary Optimization, vol. 65, no. 9, 2022.

[2] C. Luo, X. Li, Y. Liao et al., "Design of End-Iron-Free Voice Coil Motor with Appropriate PM Length Ratio," IEEE Transactions on Energy Conversion, vol. 35, no. 2, pp. 1139-1146, 2020.

[3] T. J. Teo, H. Zhu, S.-L. Chen et al., "Principle and Modeling of a Novel Moving Coil Linear-Rotary Electromagnetic Actuator," IEEE Transactions on Industrial Electronics, vol. 63, no. 11, pp. 6930-6940, 2016.

[4] G. Wang, R. Gao, Q. Wang et al., "Thermal analysis method of electromagnetic linear actuator based on Multiphysics coupling model," International Journal of Applied Electromagnetics and Mechanics, vol. 67, no. 1, pp. 1-17, 2021.

[5] U. Birbilen, and I. Lazoglu, "Design and Analysis of a Novel Miniature Tubular Linear Actuator," IEEE Transactions on Magnetics, vol. 54, no. 4, pp. 1-6, 2018.

[6] S. Wu, Z. Jiao, L. Yan et al., "Development of a direct-drive servo valve with high-frequency voice coil motor and advanced digital controller," IEEE/ASME Transactions on Mechatronics, vol. 19, no. 3, pp. 932-942, 2014.

[7] L. Yang, Z. Xu, L. Liu et al., "A Tubular PM Linear Generator With a Coreless Moving-Coil for Free-Piston Engines," IEEE Transactions on Energy Conversion, vol. 34, no. 3, pp. 1309-1316, 2019.

[8] C. Noergaard, M. M. Bech, J. H. Christensen et al., "Modeling and Validation of Moving Coil Actuated Valve for Digital Displacement Machines," IEEE Transactions on Industrial Electronics, vol. 65, no. 11, pp. 8749-8757, Nov, 2018.

[9] L. Yan, L. Zhang, Z. Jiao et al., "Armature Reaction Field and Inductance of Coreless Moving-Coil Tubular Linear Machine," IEEE Transactions on Industrial Electronics, vol. 61, no. 12, pp. 6956-6965, 2014.

[10] X. Zhao, and S. Niu, "Development of a Novel Transverse Flux Tubular Linear Machine With Parallel and Complementary PM Magnetic Circuit for Precision Industrial Processing," IEEE Transactions on Industrial Electronics, vol. 66, no. 6, pp. 4945-4955, 2019.

[11] X. Li, W. Xu, C. Ye et al., "Comparative Study of Transversal-Flux Permanent-Magnetic Linear Oscillatory Machines for Compressor," IEEE Transactions on Industrial Electronics, vol. 65, no. 9, pp. 7437-7446, 2018.

[12] S. Wu, X. Zhao, X. Li et al., "Preliminary Design and Optimization of Toroidally Wound Limited Angle Servo Motor Based on a Generalized Magnetic Circuit Model," IEEE Transactions on Magnetics, vol. 52, no. 9, pp. 1-9, 2016.

[13] Z. Jiao, T. Wang, and L. Yan, "Design of a Tubular Linear Oscillating Motor With a Novel Compound Halbach Magnet Array," IEEE/ASME Transactions on Mechatronics, vol. 22, no. 1, pp. 498-508, 2017.

[14] P. Hekmati, R. Yazdanpanah, M. Mirsalim et al., "Radial-Flux Permanent-Magnet Limited-Angle Torque Motors," IEEE Transactions on Industrial Electronics, vol. 64, no. 3, pp. 1884-1892, 2017.

[15] T. Wang, L. Yan, Z. Jiao et al., "Analytical modeling of linear oscillating motor with a mixed method considering saturation effect," Sensors and Actuators A: Physical, vol. 234, pp. 375-383, 2015.

[16] M.-F. Hsieh, and Y.-C. Hsu, "A Generalized Magnetic Circuit Modeling Approach for Design of Surface Permanent-Magnet Machines," IEEE Transactions on Industrial Electronics, vol. 59, no. 2, pp. 779-792, 2012.

[17] S. Wu, X. Zhao, C. Li et al., "Multiobjective Optimization of a Hollow Plunger Type Solenoid for High Speed On/Off Valve," IEEE Transactions on Industrial Electronics, vol. 65, no. 4, pp. 3115-3124, 2018.

[18] S. Wu, X. Zhao, Z. Jiao et al., "Multi-Objective Optimal Design of a Toroidally Wound Radial-Flux Halbach Permanent Magnet Array Limited Angle Torque Motor," IEEE Transactions on Industrial Electronics, vol. 64, no. 4, pp. 2962-2971, 2017.